



THE UNIVERSITY *of* EDINBURGH

Edinburgh Research Explorer

Titanium Nitride-Supported Platinum with Metal-Support Interaction for Boosting Photocatalytic H₂ Evolution of Indium Sulfide

Citation for published version:

Liu, S, Qi, W, Adimi, S, Guo, H, Weng, B, Attfield, JP & Yang, M 2021, 'Titanium Nitride-Supported Platinum with Metal-Support Interaction for Boosting Photocatalytic H₂ Evolution of Indium Sulfide', *ACS Applied Materials and Interfaces*, vol. 13, no. 6, pp. 7238-7247. <https://doi.org/10.1021/acsami.0c20919>

Digital Object Identifier (DOI):

[10.1021/acsami.0c20919](https://doi.org/10.1021/acsami.0c20919)

Link:

[Link to publication record in Edinburgh Research Explorer](#)

Document Version:

Peer reviewed version

Published In:

ACS Applied Materials and Interfaces

General rights

Copyright for the publications made accessible via the Edinburgh Research Explorer is retained by the author(s) and / or other copyright owners and it is a condition of accessing these publications that users recognise and abide by the legal requirements associated with these rights.

Take down policy

The University of Edinburgh has made every reasonable effort to ensure that Edinburgh Research Explorer content complies with UK legislation. If you believe that the public display of this file breaches copyright please contact openaccess@ed.ac.uk providing details, and we will remove access to the work immediately and investigate your claim.



Titanium nitride-supported platinum with metal–support interaction for boosting photocatalytic H₂ evolution of indium sulfide

Siqi Liu^{†,‡}, Weiliang Qi^{†,‡}, Samira Adimi^{†,‡}, Haichuan Guo^{†,‡}, Bo Weng^{||}, John Paul Attfield^{*§} and Minghui Yang^{*†,‡}*

[†]Ningbo Institute of Materials Technology & Engineering, Chinese Academy of Sciences, Ningbo 315201, P.R. China.

[‡]Center of Materials Science and Optoelectronics Engineering, University of Chinese Academy of Sciences, Beijing 100049, P.R. China.

[§]Centre for Science at Extreme Conditions and School of Chemistry, University of Edinburgh, King's Buildings, Edinburgh, UK.

^{||}cMACS, Department of Microbial and Molecular Systems, KU Leuven, Celestijnenlaan 200F, 3001 Leuven, Belgium.

ABSTRACT.

Metal-support interaction strongly influences the catalytic properties of metal-based catalysts. Here, titanium nitride (TiN) nanospheres are shown to be an outstanding support, for tuning the electronic property of platinum (Pt) nanoparticles and adjusting the morphology of indium sulfide (In_2S_3) active components, forming flower-like core-shell nanostructures ($\text{TiN-Pt@In}_2\text{S}_3$). The strong metal-support interaction between Pt and TiN through the formation of Pt-Ti bonds favours the migration of charge carrier and leads to the easy reducibility of TiN-Pt, thus improving the photocatalytic atom efficiency of Pt. The $\text{TiN-Pt@In}_2\text{S}_3$ composite shows reduction of Pt loading by 70% compared to the optimal Pt-based system. Besides, the optimal $\text{TiN-Pt@In}_2\text{S}_3$ composite exhibits H_2 evolution rate 4 times that of a Pt reference. This increase outperforms all other supports reported thus far.

KEYWORDS. Metal-support interaction; Transition metal nitride; Platinum; Photocatalytic H_2 evolution; Core-shell nanostructure.

1. INTRODUCTION

Direct solar-to-fuel conversion has the potential to ameliorate the growing energy crisis.¹⁻² Hydrogen production from photocatalytic water splitting provides an attractive approach for converting intermittent solar energy into a storable and clean chemical fuel.³⁻⁴ Despite several attempts to develop photocatalytic hydrogen production systems, low efficiency continues to be a challenge because of therapid recombination of charge-carriers.⁵⁻⁶ Hence co-catalysts are required to suppress charge carrier recombination and provide effective proton reduction sites for achieving highly efficient photocatalytic hydrogen production.⁷ Practical photocatalysts use Pt as the cocatalyst to accelerate the H₂ evolution reaction as it affords the highest exchange current density and has a low Tafel slope ($\sim 30 \text{ mV dec}^{-1}$).⁸⁻⁹ However, low abundance and high cost associated with Pt limits its large scale application.¹⁰

In this regard, minimizing the metal Pt loading while simultaneously improving the atom mass efficiency of Pt is a feasible strategy to striking a balance between photocatalytic activity and fabrication cost. Downsizing Pt nanoparticles to clusters or even single atoms provides an effective approach to improve the atom efficiency of Pt in photocatalytic hydrogen production.¹¹⁻¹² For example, a single atom Pt co-catalyst led to significantly enhanced photocatalytic H₂ generation, 8.6 times higher than that of Pt nanoparticles (on per Pt atom basis).¹³ However, the complex synthesis process and easy aggregation occurring during reaction limits the practical application of such single atom-based materials. Generally, the interaction between metal species and the support strongly influences the performance of catalysts.¹⁴ Thus, introducing a support component for Pt forming metal-support interaction (MSI) is another efficient way to enhance Pt atom efficiency.¹⁵ Charge transfer from metal nanoparticles to support could induce the restruction of metal nanoparticles and formation of specific metal-support interfaces, which can improve the photocatalytic performance.¹⁶⁻¹⁷ For example, carbon-based materials as Pt nanoparticle supports have been reported by different groups.¹⁸ Zhang and co-workers using SiO₂ nanosphere as a support couple with Pt nanoparticles fabricating SiO₂/Pt/TiO₂ nanocomposites.¹⁹ In addition to Schottky-junction-driven electron transfer from TiO₂ to Pt, Pt nanoparticles also produce hot electrons by recycling the scattered visible and near-infrared (vis-NIR) light of the support. This synergistically increases the electron density over Pt nanoparticles and thus promotes photoactivity of the composite for hydrogen production under simulated

sunlight. Nevertheless, the supports reported thus far have offered little opportunity to reduce Pt loading. Therefore, novel support materials are needed to improve Pt atom efficiency.

Transition metal nitrides (TMNs) have been reported as alternative catalysts to Pt due to the introduction of negatively charged nitrogen atoms that modify the d-band density of the parent metals.²⁰⁻²² TiN is one of the few TMN materials that exists in nature; it possesses notable properties such as high thermal stability, chemical inertness, and electrical and thermal conductivities.²³⁻²⁴ Furthermore, TiN has been reported to be an effective support material for Pt minimization or replacement in the field of electrocatalysis.²⁵⁻²⁷ As large numbers of efficient electrocatalysts including Pt are also utilized as efficient co-catalysts in photocatalysis, TiN has the potential for being an effective support for improving atom efficiency of Pt in photocatalytic hydrogen production.

Herein, we have prepared TiN nanosphere as a support to on one hand tune the electronic structures and improve the atom efficiency of Pt nanoparticle, on the other hand promote the dispersion of the In₂S₃ active component for forming flower-like core-shell nanostructures (TiN-Pt@In₂S₃). The formation of the bonding between Pt and Ti atoms results in strong metal-support interaction between Pt and TiN. It positively affects the co-catalytic performance of TiN-Pt in hydrogen production and leads to the efficient charge carrier separation and easy reducibility of TiN-Pt. Therefore, the optimal TiN-Pt@In₂S₃ composite exhibits H₂ evolution rate of 48.9 $\mu\text{mol g}^{-1} \text{h}^{-1}$, which is 4 times higher than the Pt-based reference catalyst (12.7 $\mu\text{mol g}^{-1} \text{h}^{-1}$). This increase outperforms all other supports reported thus far. Besides, the TiN-Pt@In₂S₃ sample also shows reduction of Pt loading by 70% as compared to the optimal Pt-based system.

2. EXPERIMENTAL SECTION

Synthesis of TiN nanospheres. TiN nanospheres were synthesized via thermal ammonolysis of TiO₂ nanospheres. 1.98 g Hexadecylamine (HDA) was dissolved in 200 mL absolute ethanol with 1.6 mL deionized water. The mixture was stirred for 30 min. Thereafter 4.5 mL of Titanium (IV) isopropoxide (TIP) was used as the titanium source. It was added into the mixture quickly, and vigorously stirred. The white precursor suspension was kept static for 18 h and washed thoroughly with ethanol. The sample thus obtained was dried at 60 °C for 12h in an oven. The

TiO₂ nanospheres with different sizes have also been synthesized. TiO₂ precursors with small size are fabricated *via* the same method with this manuscript except for keeping static for 18 h. Subsequently the samples were transferred to a quartz boat and nitrated in NH₃ flow (99.999%) using a flow rate of 200 sccm at 700 °C. This was done with a heating rate of 5 °C min⁻¹ to reach 700 °C; there after the temperature was maintained for 4h. The sample was then cooled down to the room temperature in the same flow.

Synthesis of TiN-Pt composites. In order to synthesize the TiN-Pt composites, 30 mg of TiN was dispersed into 30 mL ethylene glycol. Subsequently formation of dispersion was ensured using ultrasonication for 10 min. The suspension was then transferred to a 50 mL teflon reactor. A certain amount (300 µL, 1 mL, 3 mL and 5 mL) of 50 mM chloroplatinic acid (aq.) solution was added into the teflon reactor. The suspension was then stirred for 2 h. The pH of the suspension was then adjusted to 8-9; the suspension was poured into a 100 mL teflon-lined autoclave and heated at 150 °C for 8 h. The product was then centrifuged and washed several times with deionized water and ethanol. The product was then dried at 60 °C for 12 h in an oven.

Synthesis of flower-like TiN@In₂S₃ and TiN-Pt@In₂S₃ core-shell composites. In a typical procedure for the synthesis of TiN@In₂S₃ composites, different amounts of TiN nanospheres were dispersed into 100 mL anhydrous alcohol and dispersed using ultrasound for 5 min. 50 mg CTAB was then added to the suspension and ultrasonically dispersed for 10 min. After that, 360 mg TAA and 707 mg InCl₃·4H₂O were in turn dissolved in above mixed solution and ultrasonically dispersed for 10 min, respectively. Finally, the solution obtained was transferred to a round flask and refluxed at 95 °C for 120 min. After cooling, the as-synthesized products were washed thoroughly with ethanol and dried in an oven at 60 °C overnight. TiN-Pt@In₂S₃ composites were synthesized using the same procedure as the one used to make flower-like TiN@In₂S₃ core-shell structures. The only difference was that the TiN related steps was eliminated completed. The synthesis of the other contrast samples and composites are shown in the Supporting Information (SI).

Characterization. The crystal structure for solid samples were characterized using an X-ray diffractometer (XRD, Rigaku Miniflex 600, Japan). Raman spectra were obtained on a confocal microprobe Raman system (Renishaw inVia Reflex). The diffuse reflectance spectra (DRS) of

the samples were measured using a UV-Vis spectrophotometer (Hitachi U-3900, Japan) equipped with an integrating sphere. Morphologies of the samples and EDX spectra were characterized using a field-emission scanning electron microscope (FE-SEM, Hitachi S4800, Japan). The transmission electron microscopy (TEM) images and high-resolution transmission electron microscopy (HRTEM) images were obtained using a JEOL model JEM 2010 EX instrument. Elemental mapping was characterized by Talos F200x instrument. Temperature-programmed hydrogen reduction (H_2 -TPR) was characterized using Micromeritics 2920 adsorption apparatus. X-ray photoelectron spectroscopy (XPS) and Ultraviolet photoelectron spectroscopy (UPS) were collected using an AXIS Ultra DLD (Shimadze, Japan) spectrometer with Al K_α excitation (1486.6 eV). The photo-electrochemical properties of the samples were conducted in a homemade three electrode system. The details were shown in **SI**.

Photoactivity testing. The photocatalytic hydrogen evolution performances of the samples were tested in a commercial Perfect light system using gas chromatograph for the monitoring of hydrogen. The details were shown in **SI**.

Computational details. The Density Functional Theory (DFT) was performed for structural relaxation and electronic properties in a basis set of plane waves with the Projector Augmented Wave (PAW) pseudo-potentials for electron-core interactions²⁸ using Quantum Espresso Package.²⁹ We used the crystal structure as determined using analysis of X-ray diffraction patterns. The full relaxation of unit cells and atomic coordinates were allowed until the total energy scf accuracy of 10^{-6} eV atom⁻¹. The cut off for the residual force was 0.001 eV/Å, with 50 Ry cutoff energy and a $6\times 6\times 6$ k-point mesh, which was generated using the Monkhorst Pack method.³⁰ The BFGS quasi-newton algorithm³¹ is used for calculating the ground state geometry of structure, position and lattice volume to be changed, and structure is fully relaxed until the total force is less than 10^{-4} .

3. RESULTS AND DISCUSSION

Structural and morphology of TiN-Pt. The TiN nanospheres were prepared using TiO_2 nanospheres as the precursor through the nitriding treatment in NH_3 atmosphere, as shown in **Scheme S1** (Supporting Information). The TiO_2 nanospheres were fabricated *via* a precursor hydrolysis method, which exhibits uniform and spherical morphology with diameters around 516

nm and with fairly smooth surfaces (**Figure S1a and b**, Supporting information). After being treated in NH_3 atmosphere at 700°C for 4 h, the TiO_2 nanospheres completely converts to cubic TiN, as confirmed by X-ray diffractometer (XRD) in **Figure S2**, and the smooth nanospheres shrank to around 317 nm resulting in rough surfaces during this nitriding process (**Figure S1c and d**). The transmission electron microscopy (TEM) images shown in **Figure S3** exhibit that TiN nanospheres are composed of nanoparticles along with small pores, and the measured lattice spacing of 0.211 nm is consistent with the d-spacing of the (200) plane of cubic TiN. Then, the nitrogen (N_2) adsorption–desorption isotherms have been performed to investigate the surface area of TiO_2 and TiN. As illustrated in **Figure S4** and **Table S1**, TiO_2 exhibits the type IV isotherm with a typical H3 hysteresis loop characteristic of mesoporous solids. Its specific BET surface area and pore size are $11.7\text{ m}^2\text{ g}^{-1}$ and $0.04\text{ cm}^3\text{ g}^{-1}$, respectively. After the nitriding process, the specific BET surface area and pore size of TiN enhance to $47.8\text{ m}^2\text{ g}^{-1}$ and $0.16\text{ cm}^3\text{ g}^{-1}$, respectively. This obvious variation attributes to the rough surfaces of TiN nanospheres, which is observed in TEM images (**Figure S3**).

X-ray photoelectron spectroscopy (XPS), a sensitive surface characterization technique, was employed to analyze the surface chemical composition. Survey XPS spectrum in **Figure S5a** shows the presence of Ti, N and O elements in the TiN nanospheres. As mirrored in **Figure S5b**, two 2p peaks with shoulder profile in the high-resolution spectrum of the core level of Ti 2p in TiN was consistent with values in literature.³² This confirms the formation of TiN. The Ti $2p_{3/2}$ and Ti $2p_{1/2}$ peaks with binding energies of 455.6 and 461.1 eV were ascribed to Ti-N, and the shoulder peaks at 456.8, 462.5, 458.4 and 464.0 eV for Ti $2p_{3/2}$ and Ti $2p_{1/2}$ were assigned to O-Ti-N and Ti-O, respectively.³³⁻³⁴ The existence of the O-Ti-N bond and Ti-O bond indicated an ultrathin oxide layer on the surface of TiN nanospheres. The N 1s spectrum of the sample in **Figure S5c** was fitted using three peaks which match with the binding energy of Ti-N (396.1 eV), O-Ti-N (397.2 eV), and adsorbed N (399.2 eV),³⁵⁻³⁶ respectively. This is in agreement with Ti 2p results, further confirming the formation of TiN nanospheres.

Thereafter, using an in-situ hydrothermal method, Pt nanoparticles (NPs) were loaded onto the surface of TiN support, forming TiN-Pt composite. XRD analysis in **Figure 1a** confirms the formation of cubic TiN and Pt phases (both have space group of Fm-3m) in TiN-Pt sample. No secondary impurity phases are observed. The SEM image of the TiN-Pt sample in **Figure S6a**

and **S6b** shows that the Pt NPs were uniformly dispersed on the surface of TiN nanospheres by the ethylene glycol reduction process (**Scheme S1**). The average size of Pt NPs is calculated at around 3.1 nm (**Figure S6c** and **S6d**). The measured lattice spacing of 0.211 and 0.227 nm in **Figure 1b-f** are consistent with the d-spacing of the (200) and (111) plane of cubic TiN and Pt, respectively. Besides, a close contact between TiN and Pt is observed in HRTEM, indicating a metal to support interaction. The elements of Ti, N, and Pt are evenly detected in the elemental mapping (**Figure 1g**). It clearly reveals the uniform distribution of Pt nanoparticles on the surface of TiN support. Moreover, energy dispersive X-ray (EDX) result has revealed a weight ratio of Pt to TiN support of 1:1, as illustrated in **Figure S6e**. It is similar with the feed ratio in the synthesis process, also well corresponding the XRD refinement result of 51.9 : 48.1.

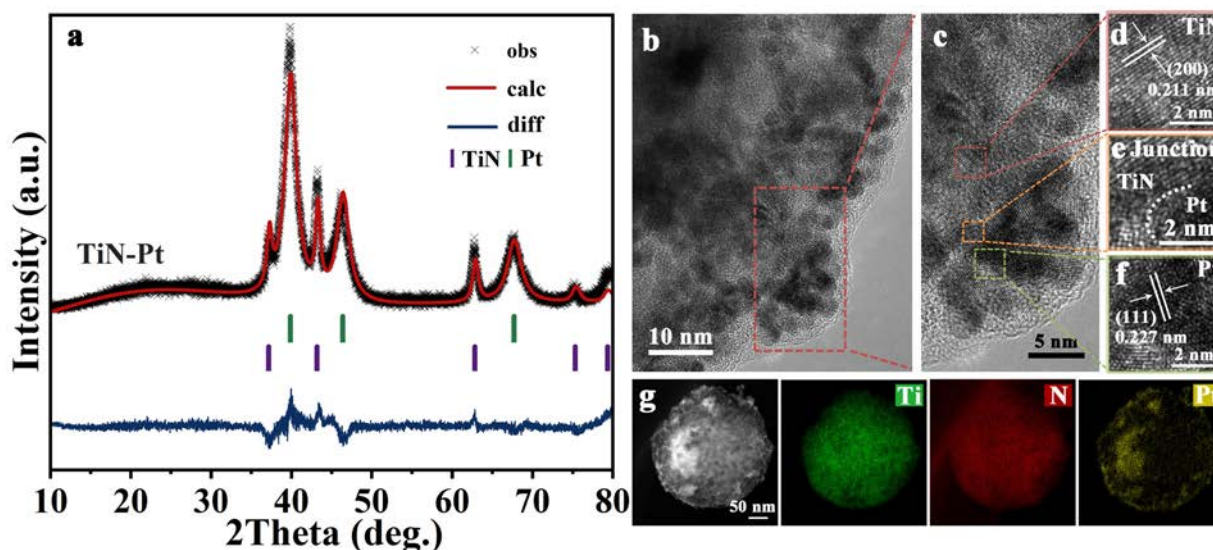


Figure 1. (a) Rietveld refined XRD pattern of TiN-Pt composite. (b, c) TEM images of TiN-Pt composite. (d, e, f) High-resolution TEM images of selected regions of the particle. The lattice spacing of 0.211 and 0.227 nm are consistent with the d-spacing of the (200) and (111) plane of cubic TiN and cubic Pt, respectively. The junction between TiN and Pt can be clearly observed. (g) TEM mapping of TiN-Pt. EDX mapping images of Ti, N and Pt show a homogeneous elemental distribution. a.u., arbitrary units.

Elaboration of TiN-Pt@In₂S₃. Using the TiN and TiN-Pt nanospheres as templates, the composites of TiN@In₂S₃ and TiN-Pt@In₂S₃ have been synthesized, as illustrated in **Scheme S1b** and **c**. The SEM images of TiN@In₂S₃ and TiN-Pt@In₂S₃ composites in **Figure 2a** and

Figure S7 show the similar flower-like nanostructures, among which the In_2S_3 nanosheets with thickness of ~ 15 nm are uniformly coated onto the surface of the TiN and TiN-Pt nanospheres support. TEM images in **Figure S8a-c** and **Figure 2d** further confirm the flower-like core-shell nanostructures of $\text{TiN}@ \text{In}_2\text{S}_3$ and $\text{TiN-Pt}@ \text{In}_2\text{S}_3$, in which the TiN and TiN-Pt nanospheres are enwrapped by In_2S_3 nanosheets with intimate interfacial contact. The HRTEM image in **Figure 2d** shows a d spacing of 0.286 nm that matches with the interspacing of (400) planes of cubic In_2S_3 phase. However, d spacing of TiN cannot be detected due to the thick shell of In_2S_3 nanosheets. In addition, **Figure 2b** shows the overlapping TEM mapping of various elements, including In, S, Ti, N and Pt, also indicating the flower-like core-shell architecture formation of the $\text{TiN-Pt}@ \text{In}_2\text{S}_3$ nanocomposites. Similar element distribution has also been observed over the $\text{TiN}@ \text{In}_2\text{S}_3$ nanocomposites (**Figure S8d**). Therefore, based on the above analyses, it is reasonable to infer that the In_2S_3 nanosheets are intimately coupled with the TiN and TiN-Pt nanospheres featuring a flower-like core-shell nanostructure. For the purpose of comparison, blank In_2S_3 , and In_2S_3 -Pt samples have also been prepared. Importantly, without the addition of TiN nanosphere support, blank In_2S_3 and In_2S_3 -Pt exhibit aggregation with irregular morphology (**Figure S9**). The morphology differences of the samples suggest that TiN support could effectively promote the dispersion of the In_2S_3 active component.

The crystal structures of the $\text{TiN}@ \text{In}_2\text{S}_3$ and $\text{TiN-Pt}@ \text{In}_2\text{S}_3$ nanocomposites have been investigated by XRD, as shown in **Figure 2c** and **Figure S10**. All the samples exhibit similar XRD patterns. The diffraction peaks of the sample mainly corresponding to the cubic In_2S_3 phase (JCPDS No. 32-0456). A weak diffraction peak at 39.8° , corresponding to the (111) lattice planes of the cubic Pt (JCPDS No. 03-065-2868) can be observed when the addition amount is 3wt%. The small diffraction peak located at 42.8° demonstrates the presence of TiN, and corresponding to the (200) lattice planes of the TiN (JCPDS No. 01-087-0632).

The surface properties of the as-prepared nanocomposites have been studied by XPS spectra, as shown in **Figure S11**. The fully scanned spectrum of In_2S_3 -based samples reveals the presence of elements such as In, S, O and C on the surface of the samples (**Figure S11a**). However, TiN and Pt elements have not been observed due to the thick shell of In_2S_3 nanosheets. **Figure S11b** and **S11c** display the typical high-resolution XPS spectra of In 3d and S 2p of the samples, respectively.³⁷ The two strong peaks at binding energies of 452.6 and 445 eV for In 3d are

assigned to the In 3d_{3/2} and In 3d_{5/2}, while the two strong peaks at 161.7 and 162.9 eV in the S 2p spectrum being attributed to the S 2p_{3/2} and S 2p_{1/2}, respectively.³⁸⁻³⁹ In addition, the optical properties of the samples are determined by UV-Vis diffuse reflectance spectra (DRS) measurement as displayed in **Figure 2e** and **Figure S12**. It can be seen that blank In₂S₃ exhibits intrinsic band gap absorption with an absorption edge onset at 580 nm, corresponding to the band gap (E_g) of about 2.1 eV.⁴⁰ The addition of TiN and TiN-Pt nanospheres can on one hand increase the light absorption intensity in the visible light region ranging from 580 to 800 nm as compared to blank In₂S₃, which can be ascribed to the broad background absorption of TiN in the visible light region (**Figure S13**).⁴¹ On the other hand, the slight red shifts of the edge absorption are observed in a series of nanocomposites as compared to blank In₂S₃, which could be attributed to the strong interaction between cocatalyst and In₂S₃ nanosheets.⁴²

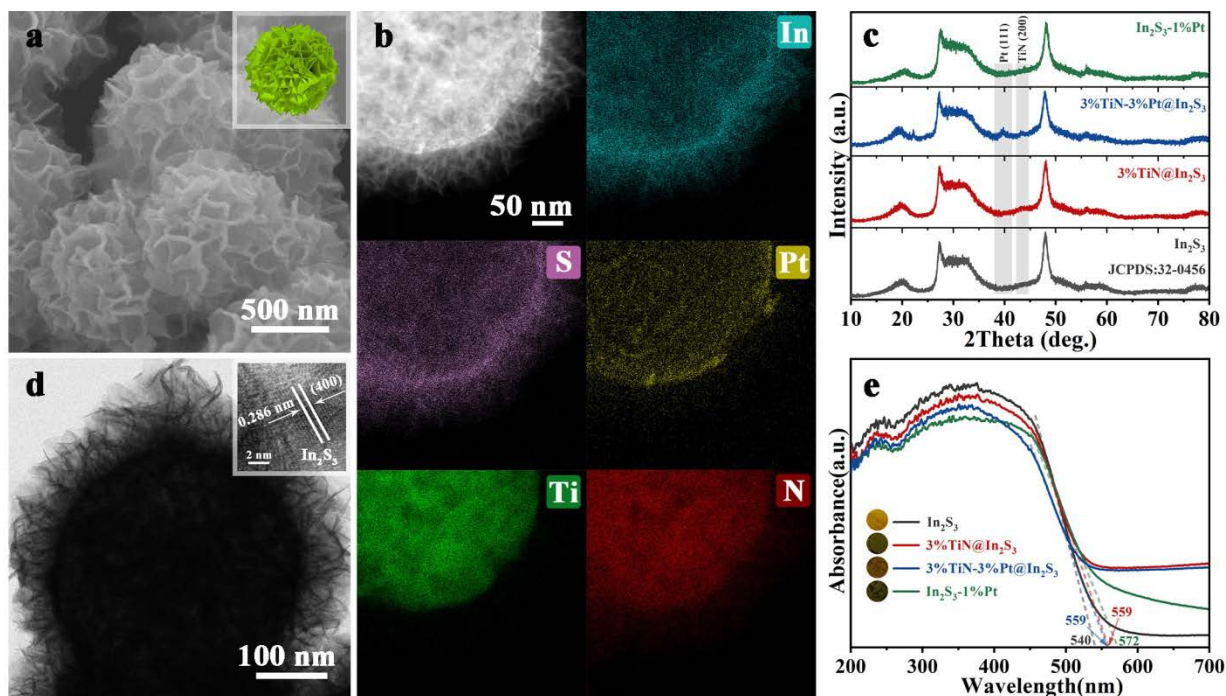


Figure 2. (a) SEM image of the TiN-Pt@In₂S₃ composite. (b) TEM mapping of the TiN-Pt@In₂S₃ composite. (c) X-ray diffraction (XRD) pattern of as-prepared samples. (d) TEM image of the TiN-Pt@In₂S₃ composite. (e) UV-vis absorption spectra of as-prepared samples.

Visible-light-driven H₂ evolution properties. The photocatalytic H₂ evolution over the blank In₂S₃, a series of TiN@In₂S₃ and TiN-Pt@In₂S₃ core-shell nanostructures was performed under

visible light irradiation ($\lambda > 420$ nm) using lactic acid as the hole scavengers. As shown in **Figure S14**, controlled experiments have shown that only In_2S_3 exhibits photocatalytic H_2 evolution activity under visible light irradiation. Neither pure TiN nor TiN-Pt shows photocatalytic H_2 evolution performance. Without light irradiation, none of the samples shows photocatalytic activity. The above results indicate that the In_2S_3 is the active component, and both of TiN and TiN-Pt are utilized as co-catalysts. In addition, the H_2 evolution reaction is driven by light irradiation. As shown in **Figure 3a**, blank In_2S_3 show a H_2 evolution rate of $2.9 \mu\text{mol g}^{-1} \text{h}^{-1}$. With addition of TiN nanospheres, a series of $\text{TiN@In}_2\text{S}_3$ core-shell nanostructures display obvious enhancement of H_2 evolution rate as compared to blank In_2S_3 . The optimal addition amount of TiN is demonstrated to be 3 wt% (**Figure S15a**), and the 3 wt% $\text{TiN@In}_2\text{S}_3$ composite exhibits the H_2 evolution rates of $5.3 \mu\text{mol g}^{-1} \text{h}^{-1}$ (**Figure 3a**). Notably, further increasing the content of TiN to 5 wt% leads to a gradual decrease of H_2 evolution activity. This originates from the “shielding effect” of TiN; that is opacity TiN will weaken the light irradiation depth through the depth of the reaction solution. This would unavoidably restrict the efficiency of TiN in promoting the photoactivity of $\text{TiN@In}_2\text{S}_3$ composite.⁴³

The introduction of different amount of Pt NPs results in a significant improvement in the photocatalytic H_2 production activity over the $\text{TiN-Pt@In}_2\text{S}_3$ composites. Controlled experiments have eliminated the size effect of Pt nanoparticles in improving the photocatalytic activity of $\text{TiN-Pt@In}_2\text{S}_3$ nanocomposites. As shown in **Figure S16**, different loading amounts of Pt nanoparticles in Pt-TiN exhibit similar particle size of Pt. Besides, the size of TiN support has also been adjusted. It can be seen in **Figure S17**, that with loading similar amount of Pt, $\text{TiN-Pt@In}_2\text{S}_3$ nanocomposites with different size of TiN show similar photocatalytic activity under visible light irradiation. As displayed in **Figure 3a** and **Figure S15b**, the optimal 3 wt%TiN-3 wt%Pt@ In_2S_3 exhibits the highest H_2 evolution rate of $48.9 \mu\text{mol g}^{-1} \text{h}^{-1}$. Notably, the optimal In_2S_3 -1 wt%Pt sample shows H_2 evolution rate of $12.7 \mu\text{mol g}^{-1} \text{h}^{-1}$ (**Figure S15c**). This suggests that the photocatalytic H_2 generation rate over the 3 wt%TiN-3 wt%Pt@ In_2S_3 sample is almost 9 times and 4 times higher than of 3 wt%TiN@ In_2S_3 and In_2S_3 -1 wt%Pt composites, respectively. In fact, it is to be noted that Pt NPs are generally utilized as a standard co-catalyst to determine the performances of other co-catalysts. As shown in **Table S2**, as compared to all previously reported Pt-replacement co-catalysts and Pt-modified systems, the H_2 evolution enhancement

observed with TiN-Pt hybrid is the most efficient, indicating the effectiveness of TiN as a Pt support.

Furthermore, it is quite interesting to find that the optimal weight addition ratio of Pt for the Pt@In₂S₃ and TiN-Pt@In₂S₃ composites are 1% and 3%, respectively. Generally, the optimal weight addition ratio of Pt for metal-semiconductor composite photocatalysts is less than 1% for achieving the proper synergy interaction between the semiconductor and Pt.⁴⁴⁻⁴⁵ As discussed above, opacity of TiN nanospheres also have a “shielding effect” similar to Pt. It is proposed that the recombination centers’ role of Pt is inhibited by addition of TiN nanospheres through intimate interfacial contact between Pt and TiN. This hypothesis is indirectly evidenced by a control experiment. Pt nanoparticles are loaded onto the surface of 3 wt% TiN@In₂S₃ composite by the same method with synthesis of In₂S₃-Pt, forming 3 wt% TiN@In₂S₃-3 wt% Pt nanocomposite. Due to the enhanced spatial separation of photo-carriers excited from In₂S₃, ternary TiN@In₂S₃-Pt nanocomposite exhibits higher H₂ evolution rate (25.1 μmol g⁻¹ h⁻¹) than that of binary In₂S₃-Pt (**Figure 3a**). However, this is still lower than that of TiN-Pt@In₂S₃. It further reveals the positive role of interaction between Pt and TiN in the TiN-Pt@In₂S₃ nanocomposites. In fact, this positive role of interaction between Pt and TiN also benefits to other semiconductor-based systems. As shown in **Figure S18**, TiN-Pt@TiO₂ nanocomposites also exhibit similar trend of enhanced photocatalytic performances as compared to Pt-TiO₂ and TiN@TiO₂ nanocomposites.

It is well known that the most severe limitation of utilization of Pt cocatalysts in photocatalytic artificial photosynthesis is their high cost. Therefore, maximizing the mass efficiency of Pt in photocatalytic water splitting is more important for their large-scale application. It is to be noted that 3 wt% TiN-0.3 wt% Pt@In₂S₃ composite exhibits similar H₂ evolution rate of 13.2 μmol g⁻¹ h⁻¹ when compared to optimal In₂S₃-Pt (12.7 μmol g⁻¹ h⁻¹). This means that the loading amount of Pt NPs can be decreased to 30 wt%, suggesting the significant increased mass activity of TiN-Pt as compared with that of Pt. **Figure 3b** gives the relative photocatalytic activity on the per gram Pt basis. Clearly, 3 wt% TiN-0.3 wt% Pt@In₂S₃ exhibits highest H₂ evolution rate of 4397.5 μmol g⁻¹ h⁻¹ on per gram Pt, which is more than 3 times higher than that of In₂S₃-1 wt% Pt. Collectively, these photocatalytic activity results suggest that TiN nanospheres can be utilized as

a desirable support for Pt nanoparticle in improving the mass efficiency of Pt, resulting in Pt minimization.

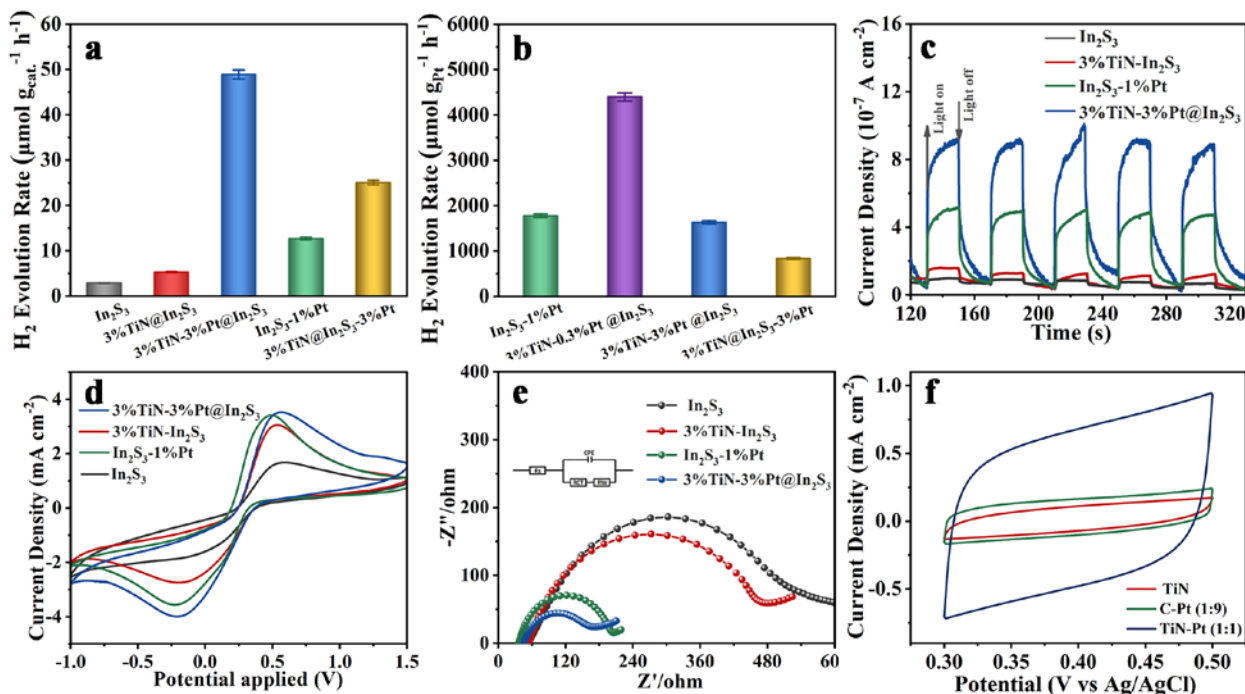


Figure 3. (a) The average rates of H_2 evolution under visible light irradiation ($\lambda > 420 \text{ nm}$, lactic acid as the sacrificial agents) over different samples. (b) H_2 evolution rates of unit mass for precious metal Pt over four different catalysts. (c) Transient photocurrent response, (d) cyclic voltammograms and (e) electrochemical impedance spectroscopy of the as-prepared four samples. (f) Specific capacitance performances of as-prepared three samples.

Photoelectrochemical (PEC) properties. A series of joint techniques have been employed to characterize the samples with optimal photoactivity to reveal the origin accounting for the photoactivity enhancement of TiN-Pt@ In_2S_3 composites as compared to that of TiN@ In_2S_3 and In_2S_3 -Pt composites. The photoelectrochemical (PEC) analysis has been performed to investigate the charge carrier transfer process over blank In_2S_3 , In_2S_3 -1 wt% Pt, 3 wt% TiN@ In_2S_3 and 3 wt% TiN-3 wt%Pt@ In_2S_3 . As shown in **Figure 3c**, the TiN-Pt@ In_2S_3 displays obvious transient photocurrent response under visible light irradiation, which is a 2-fold, 5-fold and 10-fold photocurrent enhancement as compared with In_2S_3 -Pt, TiN@ In_2S_3 and blank In_2S_3 , respectively. This is a marked improvement, which suggests the composition advantage of the TiN-Pt@ In_2S_3 nanocomposite in promoting the separation and transportation of photo-generated charge

carriers.⁴⁶ The high electrical conductivity of TiN and interaction between TiN and Pt leads to the transformation of the photo-generated electrons from the excitation of In₂S₃ to TiN and Pt, forming multi-level charge transfer. Cyclic voltammograms (CV) over blank In₂S₃, In₂S₃-1 wt% Pt, 3 wt% TiN@In₂S₃ and 3 wt% TiN-3 wt% Pt@In₂S₃ composites with obvious anodic and cathodic peaks for each sample have been observed. Since the preparation of the electrodes and electrolyte are identical for the CV curve measurement, the current density of the electrodes is related to the electron transfer rate of the electrode materials. The CV curves of different samples in **Figure 3d** follow the trend of TiN-Pt@In₂S₃ > In₂S₃-Pt > TiN@In₂S₃ > In₂S₃. It reveals that the introduction of TiN nanospheres can enhance the current densities of TiN-Pt@In₂S₃ composites as compared to that of In₂S₃-Pt composite, which is consistent with the transient photocurrent results in **Figure 3c**.

Furthermore, the electrochemical impedance spectroscopy (EIS) as a method to monitor charge transfer process on the electrode and at the contact interface between electrode and electrolyte has also been performed.⁴⁷ It can be evidently seen that the four electrodes all show semicircles at high frequencies. The TiN-Pt@In₂S₃ nanocomposite exhibits the smallest semicircular in the Nyquist plot as compared to those of TiN@In₂S₃ and In₂S₃-Pt nanocomposites (**Figure 3e**). It indicates that TiN-Pt@In₂S₃ shows enhanced charge carrier migration efficiency as compared to the TiN@In₂S₃ and In₂S₃-Pt nanocomposites. In addition, the most efficient transfer of charge carriers over the TiN-Pt@In₂S₃ nanocomposite have been further verified by the specific capacitance performance (**Figure 3f**). It is observed that the TiN-Pt electrode shows markedly enhanced specific capacitance as compared to that of Pt/carbon and pure TiN, which indicates that TiN-Pt system can store more photo-electrons from the excited active constituent, and hence enables more effective separation of photon-generated carrier as compared to pure Pt.⁴⁸⁻⁴⁹ Therefore, the above PEC results together confirm that introducing highly conductively TiN nanospheres as Pt supports is beneficial for efficiently separating and transferring the photo-generated electrons from In₂S₃, hampering the recombination of charge carriers, and thereby resulting in the higher photocatalytic efficiency of TiN-Pt@In₂S₃ nanocomposites than that of TiN@In₂S₃ and In₂S₃-Pt nanocomposites under visible light irradiation ($\lambda > 420$ nm).

Insights into the H₂ evolution mechanism. Previously calculations have predicted electron density transfer from the support to Pt in cases wherein metal-support interactions (MSI) exist.⁵⁰⁻

⁵¹ The electronic properties of Pt are affected by support and may lead to the H-spillover effects and an enhancement of the adsorption strength of small molecules on the Pt surface. This is expected to influence the catalytic performance of Pt NPs. Therefore, the interactions between the TiN and metal Pt are investigated. The Raman analysis is very sensitive to the crystallinity and microstructure of materials, which can provide detailed information about chemical structure and molecular interactions. As shown in **Figure 4a**, pure TiN exhibits the characteristic peaks at around 264, 372, 475 and 590 cm^{-1} , which can be assigned to acoustic and optical modes of TiN.⁵² The broad bands around 300 cm^{-1} can be associated with the Ti-vibrating modes and the band around 550 cm^{-1} is due to the nitrogen-associated optical modes.⁵³ After loading of Pt nanoparticles, all TiN peaks exhibit blue shift indicating that the nitride lattice is marginally perturbed due to the bonding with surface Pt atoms.⁵⁴⁻⁵⁵ Besides, two new characteristic peaks at 174 and 721 cm^{-1} , which belong to Pt-Pt stretching vibrations and Pt-O vibrations in Pt nanoparticles.⁵⁶⁻⁵⁸ **Figure S19** shows ultraviolet photoelectron spectroscopy (UPS) valence band spectra of the TiN and TiN-Pt. The valence band maximum values are determined to be approximately 2.54 eV for TiN and 3.21 eV for TiN-Pt, respectively. Clearly, the valence band of sample is shifted away from the Fermi level due to the introduction of Pt. The shift of the valence band implies shift of d-band center in the TiN-Pt composite, which further confirms the modulation in the electronic structure of the TiN-Pt as compared with that of TiN.⁵⁹ XPS results further reveal change of electronic properties of Pt nanoparticles when the TiN support is introduced. **Figure 4b** represents a high-resolution spectrum of Pt 4f in In_2S_3 -Pt and TiN-Pt@ In_2S_3 nanocomposites. The two peaks at 72.2 eV and 75.5 eV are corresponding to Pt 4f_{7/2} and Pt 4f_{5/2}, respectively.⁶⁰⁻⁶¹ These peaks are attributed to metallic Pt NPs. When introducing TiN nanospheres as a support, both Pt 4f_{7/2} and Pt 4f_{5/2} peaks in TiN-Pt@ In_2S_3 exhibit negative shift when compared to those in In_2S_3 -Pt. These shifts in core electron binding energy, called core level shifts (CLSs), have been observed in other metal-support systems.⁶² The presence of TiN results in a redistribution of charge and affects the core levels of sample.⁶³ Based on the magnitude and direction of the CLSs (-0.8 eV) and previous literature, it can be speculated that a Pt-Ti bimetallic structure has formed and causes a charge transfer from the TiN supports to Pt NPs.^{60, 64} The above characterization results suggest the successful formation of metal-support interaction between TiN and Pt nanoparticles with tunable electronic properties of Pt by TiN support.

To further understand the effect of TiN support, a detailed investigation among TiN, Pt NPs (using carbon as support), and TiN-Pt samples have been carried out. **Figure 4c** depicts the linear sweep voltammetry (LSV) curves of TiN, Pt/carbon, and TiN-Pt electrodes. As observed, the onset over-potential of TiN-Pt is lower than that of either Pt/carbon or TiN. The lower overpotential at the same current density indicates the lower potential energy loss in case of the TiN-Pt electrode; this in turn results in a higher photocatalytic activity rate for the catalyst during proton reduction reaction.⁶⁵⁻⁶⁶ This means that TiN-Pt not only reduces the recombination rate of electron-hole pairs, but also a highly active proton reduction catalyst. Temperature-programmed hydrogen reduction (H₂-TPR) results confirm the reducible properties of Pt/carbon and TiN-Pt samples. As shown in **Figure 4d**, the TPR profile of the Pt/carbon sample is composed of two H₂ consumption peaks. The first peak appears at 340 °C and the second peak appears at 400 °C. Both peaks can be assumed to be due to the reduction of the Pt species.⁶⁷⁻⁶⁸ When the Pt NPs are loaded onto the TiN support, the low-temperature H₂ consumption peak appears at 100 °C and the shoulder associated with the H₂ consumption peak negatively shifts to 315 °C. This clearly shows the easy reducibility of TiN-Pt sample as compared to Pt/carbon.⁶⁹ The above results indicate the superiority of TiN support in promoting the catalytic properties of Pt-based materials by inhibiting the recombination of charge carriers and increasing the reducibility and electron storing ability of Pt.

Density functional theory (DFT) calculation has also been employed to reveal the tenability of the electronic properties of Pt NPs. Based on the above experimental results, TiN (200) surface is chosen for theoretical investigations. As shown in **Figure S20a-c**, Pt on top of the vacancy space, with an adsorption energy of -2.42eV, is the most stable site for Pt atom on (200) surface. Pt atom makes two bonds with the surface Ti atoms. These Ti atoms could move upward in a way that (200) surface will have a zigzag form compared with the clean surface (**Figure S20c**). The related partial densities of state (DOS) is shown in **Figure S21** and **Figure 4e**. The new hybrid states associated with Pt that emerge due to interaction with TiN are observed. Covalent bond formation between Ti and Pt is indicated; this result is consistent with reports on Ti-Pt bonds.⁷⁰⁻⁷¹ To provide further insight, the Electron Localization Function (ELF) plot is shown in **Figure 4f**. The accumulation of electron density between Ti and Pt is obvious. The value of Bader charge on Pt atom is around 0.6 electrons with a negative charge on it. Therefore, there would be an enhanced occupation for the d states of Pt. This would in fact influence the sub-layer material

and lead to bonding with Ti atoms. Both the theoretical and experimental analyses collectively indicate the strong interactions between TiN support and metal Pt, which may be beneficial for the activity enhancement over the Pt NPs.

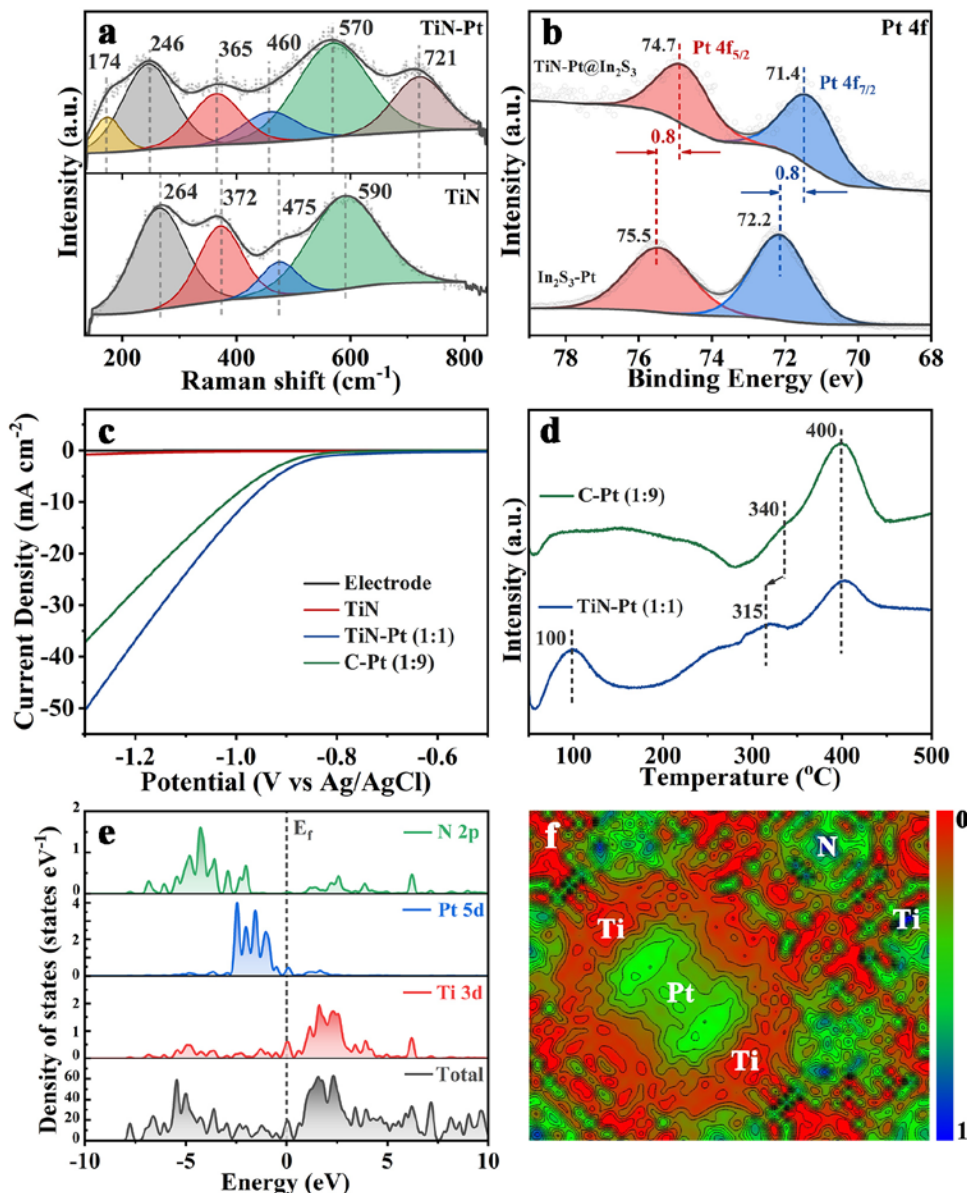


Figure. 4 (a) Raman spectra of the TiN and TiN-Pt. (b) XPS spectra of TiN-Pt@ In_2S_3 and In_2S_3 -Pt in the Pt 4f region. (c) Polarization curves of as-prepared samples. (electrode rotating speed, 1,600 r.p.m.; scan rate, 100 mV s^{-1}). (d) H_2 -TPR profiles of C-Pt and TiN-Pt samples. (e) Partial and Total DOS plots for (200)-TiN after adsorption of Pt atoms on the top-most layer. (f) Electron Localization function (ELF) plot on top (200)-TiN surface with Pt atoms adsorbed on it.

Based on the above experimental and calculation analyses, a tentative reaction mechanism for photocatalytic H₂ generation over TiN-Pt@In₂S₃ nanocomposites has been proposed, as displayed in **Figure S22**. Under visible light illumination, In₂S₃ as active component can be photo-excited to form electrons and holes from its conduction band (CB) and valence band (VB), respectively. Due to the high conductivity and low Fermi level of TiN and Pt, photo-generated electrons can transfer from the CB of In₂S₃ to the TiN-Pt, thus hampering the recombination of electrons-holes pairs. The metal-support interactions between the TiN and Pt endow the TiN-Pt with lower proton reduction overpotential and faster electron transfer capability, which efficiently promotes the photocatalytic H₂ evolution rate. Concurrently, the holes in the VB of In₂S₃ will be consumed by the hole scavenger of lactic acid. As a result, the improved transfer of photogenerated electrons significantly contribute to the remarkably enhanced photoactivity of TiN-Pt@In₂S₃ samples as compared with that of TiN@In₂S₃ and In₂S₃-Pt nanocomposites.

4. CONCLUSIONS

In summary, TiN nanospheres have been shown to be adual functional support for improving atom efficiency of Pt NPs in photocatalytic H₂ evolution and constructing TiN-Pt@In₂S₃ flower-like core-shell nanostructures. Metal-support interaction occurs due to bonding between Pt and Ti atoms on the surface of TiN. This in fact tunes the electronic property of Pt, which enables more efficient charge carrier separation and easier reducibility of TiN-Pt when compared to pure Pt NPs. When In₂S₃ is used as avisible light driven catalyst and TiN is employed as the support, the loading amount of Pt NPs can be cut down to 30%. The optimal TiN-Pt@In₂S₃ composite exhibits a H₂ evolution rate (48.9 μmol g⁻¹ h⁻¹), which is 4 times higher than the Pt reference (12.7 μmol g⁻¹ h⁻¹).

ASSOCIATED CONTENT

Supporting Information.

The Supporting Information is available free of charge on the ACS Publications website. Experimental section and supporting data.

AUTHOR INFORMATION

Corresponding Author

*E-mail addresses: bo.weng@kuleuven.be, j.p.attfield@ed.ac.uk, myang@nimte.ac.cn

Author Contributions

Siqi Liu conceived the study and wrote the initial manuscript. Weiliang Qi performed the experiments and contributed to the interpretation of characterization results. Samira Adimi contributed to the Density functional theory calculations. Haichuan Guo provided the analysis about the crystal structure. Bo Weng, John Paul Attfield and Minghui Yang provided critical feedback, helped shape the research, analysis and guided the revision of manuscript.

Notes

The authors declare no competing financial interest.

ACKNOWLEDGMENT

This work is supported by Natural Science Foundation of China (Grant No. 21471147 and 61971405) and National Key Research and Development Plan (Grant No. 2016YFB0101205). M.H. Y. would like to thank the National “Thousand Youth Talents” program of China and Ningbo 3315 program for support. S.Q. L. would like to thank for Natural Science Foundation of Zhejiang Province (LQ19B030001).

REFERENCES

- (1) Gong, J.; Li, C.; Wasielewski, M. R. Advances in solar energy conversion. *Chem. Soc. Rev.* **2019**, *48*, 1862-1864.
- (2) Kosco, J.; Bidwell, M.; Cha, H.; Martin, T.; Howells, C. T.; Sachs, M.; Anjum, D. H.; Gonzalez Lopez, S.; Zou, L.; Wadsworth, A.; Zhang, W.; Zhang, L.; Tellam, J.; Sougrat, R.; Laquai, F.; DeLongchamp, D. M.; Durrant, J. R.; McCulloch, I. Enhanced photocatalytic hydrogen evolution from organic semiconductor heterojunction nanoparticles. *Nat. Mater.* **2020**, *19*, 559-565.
- (3) Hisatomi, T.; Domen, K. Reaction systems for solar hydrogen production via water splitting with particulate semiconductor photocatalysts. *Nat. Catal.* **2019**, *2*, 387-399.
- (4) Huang, D.; Wen, M.; Zhou, C.; Li, Z.; Cheng, M.; Chen, S.; Xue, W.; Lei, L.; Yang, Y.; Xiong, W.; Wang, W. $\text{Zn}_x\text{Cd}_{1-x}\text{S}$ based materials for photocatalytic hydrogen evolution, pollutants degradation and carbon dioxide reduction. *Appl. Catal. B* **2020**, *267*, 118651.

- (5) Wang, H.; Wang, X.; Chen, R.; Zhang, H.; Wang, X.; Wang, J.; Zhang, J.; Mu, L.; Wu, K.; Fan, F.; Zong, X.; Li, C. Promoting Photocatalytic H₂ Evolution on Organic–Inorganic Hybrid Perovskite Nanocrystals by Simultaneous Dual-Charge Transportation Modulation. *ACS Energy Lett.* **2018**, *4*, 40-47.
- (6) Wang, Y.; Vogel, A.; Sachs, M.; Sprick, R. S.; Wilbraham, L.; Moniz, S. J. A.; Godin, R.; Zwiijnenburg, M. A.; Durrant, J. R.; Cooper, A. I.; Tang, J. Current understanding and challenges of solar-driven hydrogen generation using polymeric photocatalysts. *Nat. Energy* **2019**, *4*, 746-760.
- (7) Li, X.; Yu, J.; Jaroniec, M.; Chen, X. Cocatalysts for Selective Photoreduction of CO₂ into Solar Fuels. *Chem. Rev.* **2019**, *119*, 3962-4179.
- (8) Ran, J.; Zhang, J.; Yu, J.; Jaroniec, M.; Qiao, S. Z. Earth-abundant cocatalysts for semiconductor-based photocatalytic water splitting. *Chem. Soc. Rev.* **2014**, *43*, 7787-7812.
- (9) Li, Y.; Wang, H.; Xie, L.; Liang, Y.; Hong, G.; Dai, H. MoS₂ Nanoparticles Grown on Graphene: An Advanced Catalyst for the Hydrogen Evolution Reaction. *J. Am. Chem. Soc.* **2011**, *133*, 7296-7299.
- (10) Pan, Y.; Sun, K.; Liu, S.; Cao, X.; Wu, K.; Cheong, W. C.; Chen, Z.; Wang, Y.; Li, Y.; Liu, Y.; Wang, D.; Peng, Q.; Chen, C.; Li, Y. Core-Shell ZIF-8@ZIF-67-Derived CoP Nanoparticle-Embedded N-Doped Carbon Nanotube Hollow Polyhedron for Efficient Overall Water Splitting. *J. Am. Chem. Soc.* **2018**, *140*, 2610-2618.
- (11) Schweinberger, F. F.; Berr, M. J.; Dobliger, M.; Wolff, C.; Sanwald, K. E.; Crampton, A. S.; Ridge, C. J.; Jackel, F.; Feldmann, J.; Tschurl, M.; Heiz, U. Cluster size effects in the photocatalytic hydrogen evolution reaction. *J. Am. Chem. Soc.* **2013**, *135*, 13262-13265.
- (12) Gao, C.; Low, J.; Long, R.; Kong, T.; Zhu, J.; Xiong, Y. Heterogeneous Single-Atom Photocatalysts: Fundamentals and Applications. *Chem. Rev.* **2020**, *120*, 12175-12216.
- (13) Li, X.; Bi, W.; Zhang, L.; Tao, S.; Chu, W.; Zhang, Q.; Luo, Y.; Wu, C.; Xie, Y. Single-Atom Pt as Co-Catalyst for Enhanced Photocatalytic H₂ Evolution. *Adv. Mater.* **2016**, *28*, 2427-2431.
- (14) Parastaev, A.; Muravev, V.; Huertas Osta, E.; van Hoof, A. J. F.; Kimpel, T. F.; Kosinov, N.; Hensen, E. J. M. Boosting CO₂ hydrogenation *via* size-dependent metal–support interactions in cobalt/ceria-based catalysts. *Nat. Catal.* **2020**, *3*, 526-533.

- (15) Beck, A.; Huang, X.; Artiglia, L.; Zabilskiy, M.; Wang, X.; Rzepka, P.; Palagin, D.; Willinger, M. G.; van Bokhoven, J. A. The dynamics of overlayer formation on catalyst nanoparticles and strong metal-support interaction. *Nat. Commun.* **2020**, *11*, 3220.
- (16) Daelman, N.; Capdevila-Cortada, M.; Lopez, N. Dynamic charge and oxidation state of Pt/CeO₂ single-atom catalysts. *Nat. Mater.* **2019**, *18*, 1215-1221.
- (17) Willinger, M. G.; Zhang, W.; Bondarchuk, O.; Shaikhutdinov, S.; Freund, H. J.; Schlogl, R. A case of strong metal-support interactions: combining advanced microscopy and model systems to elucidate the atomic structure of interfaces. *Angew. Chem. Int. Ed.* **2014**, *53*, 5998-6001.
- (18) Wang, Y.-J.; Zhao, N.; Fang, B.; Li, H.; Bi, X. T.; Wang, H. Carbon-Supported Pt-Based Alloy Electrocatalysts for the Oxygen Reduction Reaction in Polymer Electrolyte Membrane Fuel Cells: Particle Size, Shape, and Composition Manipulation and Their Impact to Activity. *Chem. Rev.* **2015**, *115*, 3433-3467.
- (19) Zhang, N.; Qi, M.-Y.; Yuan, L.; Fu, X.; Tang, Z.-R.; Gong, J.; Xu, Y.-J. Broadband Light Harvesting and Unidirectional Electron Flow for Efficient Electron Accumulation for Hydrogen Generation. *Angew. Chem. Int. Ed.* **2019**, *58*, 10003-10007.
- (20) Xiao, X.; Wang, H.; Bao, W.; Urbankowski, P.; Yang, L.; Yang, Y.; Maleski, K.; Cui, L.; Billinge, S. J. L.; Wang, G.; Gogotsi, Y. Two-Dimensional Arrays of Transition Metal Nitride Nanocrystals. *Adv. Mater.* **2019**, *31*, e1902393.
- (21) Gu, Y.; Chen, S.; Ren, J.; Jia, Y. A.; Chen, C.; Komarneni, S.; Yang, D.; Yao, X. Electronic Structure Tuning in Ni₃FeN/r-GO Aerogel toward Bifunctional Electrocatalyst for Overall Water Splitting. *ACS Nano* **2018**, *12*, 245-253.
- (22) Chen, W.-F.; Sasaki, K.; Ma, C.; Frenkel, A. I.; Marinkovic, N.; Muckerman, J. T.; Zhu, Y.; Adzic, R. R. Hydrogen-Evolution Catalysts Based on Non-Noble Metal Nickel–Molybdenum Nitride Nanosheets. *Angew. Chem. Int. Ed.* **2012**, *51*, 6131-6135.
- (23) Kim, B. G.; Jo, C.; Shin, J.; Mun, Y.; Lee, J.; Choi, J. W. Ordered Mesoporous Titanium Nitride as a Promising Carbon-Free Cathode for Aprotic Lithium-Oxygen Batteries. *ACS Nano* **2017**, *11*, 1736-1746.
- (24) Lin, G.; Xi, S.; Pan, C.; Lin, W.; Xie, K. Growth of 2 cm metallic porous TiN single crystals. *Mater. Horiz.* **2018**, *5*, 953-960.

- (25) Tian, X.; Luo, J.; Nan, H.; Zou, H.; Chen, R.; Shu, T.; Li, X.; Li, Y.; Song, H.; Liao, S.; Adzic, R. R. Transition Metal Nitride Coated with Atomic Layers of Pt as a Low-Cost, Highly Stable Electrocatalyst for the Oxygen Reduction Reaction. *J. Am. Chem. Soc.* **2016**, *138*, 1575-1583.
- (26) Pan, Z.; Xiao, Y.; Fu, Z.; Zhan, G.; Wu, S.; Xiao, C.; Hu, G.; Wei, Z. Hollow and porous titanium nitride nanotubes as high-performance catalyst supports for oxygen reduction reaction. *J. Mater. Chem. A* **2014**, *2*, 13966.
- (27) Lale, A.; Mallmann, M. D.; Tada, S.; Bruma, A.; Özkar, S.; Kumar, R.; Haneda, M.; Francisco Machado, R. A.; Iwamoto, Y.; Demirci, U. B.; Bernard, S. Highly active, robust and reusable micro-/mesoporous TiN/Si₃N₄ nanocomposite-based catalysts for clean energy: Understanding the key role of TiN nanoclusters and amorphous Si₃N₄ matrix in the performance of the catalyst system. *Appl. Catal. B* **2020**, *272*, 118975.
- (28) Blöchl, P. E. Projector augmented-wave method. *Phys. Rev. B* **1994**, *50*, 17953-17979.
- (29) Giannozzi, P.; Baroni, S.; Bonini, N.; Calandra, M.; Car, R.; Cavazzoni, C.; Ceresoli, D.; Chiarotti, G. L.; Cococcioni, M.; Dabo, I.; Dal Corso, A.; de Gironcoli, S.; Fabris, S.; Fratesi, G.; Gebauer, R.; Gerstmann, U.; Gougoussis, C.; Kokalj, A.; Lazzeri, M.; Martin-Samos, L.; Marzari, N.; Mauri, F.; Mazzarello, R.; Paolini, S.; Pasquarello, A.; Paulatto, L.; Sbraccia, C.; Scandolo, S.; Sclauzero, G.; Seitsonen, A. P.; Smogunov, A.; Umari, P.; Wentzcovitch, R. M. QUANTUM ESPRESSO: a modular and open-source software project for quantum simulations of materials. *J. Phys.: Condens. Matter* **2009**, *21*, 395502.
- (30) Perdew, J. P.; Burke, K.; Ernzerhof, M. Generalized Gradient Approximation Made Simple. *Phys. Rev. Lett.* **1996**, *77*, 3865-3868.
- (31) Bonnans, F. J.; Gilbert, J. C.; Lemaréchal, C.; Sagastizábal, C. Numerical optimization. Theoretical and practice aspects. *IEEE T. Automat. Contr.* **2003**, *51*, 541-541.
- (32) Balogun, M.-S.; Yu, M.; Li, C.; Zhai, T.; Liu, Y.; Lu, X.; Tong, Y. Facile synthesis of titanium nitride nanowires on carbon fabric for flexible and high-rate lithium ion batteries. *J. Mater. Chem. A* **2014**, *2*, 10825-10829.
- (33) Yang, C.; Wang, H.; Lu, S.; Wu, C.; Liu, Y.; Tan, Q.; Liang, D.; Xiang, Y. Titanium nitride as an electrocatalyst for V(II)/V(III) redox couples in all-vanadium redox flow batteries. *Electrochim. Acta* **2015**, *182*, 834-840.

- (34) Yick, S.; Murdock, A. T.; Martin, P. J.; Kennedy, D. F.; Maschmeyer, T.; Bendavid, A. Tuning the plasmonic response of TiN nanoparticles synthesised by the transferred arc plasma technique. *Nanoscale* **2018**, *10*, 7566-7574.
- (35) Balogun, M.-S.; Yu, M.; Li, C.; Zhai, T.; Liu, Y.; Lu, X.; Tong, Y. Facile synthesis of titanium nitride nanowires on carbon fabric for flexible and high-rate lithium ion batteries. *J. Mater. Chem. A* **2014**, *2*, 10825-10829.
- (36) Thotiyil, M. M. O.; Kumar, T. R.; Sampath, S. Pd Supported on Titanium Nitride for Efficient Ethanol Oxidation. *J. Phys. Chem. C* **2010**, *114*, 17934-17941.
- (37) Rengaraj, S.; Venkataraj, S.; Tai, C. W.; Kim, Y.; Repo, E.; Sillanpaa, M. Self-assembled mesoporous hierarchical-like In₂S₃ hollow microspheres composed of nanofibers and nanosheets and their photocatalytic activity. *Langmuir* **2011**, *27*, 5534-5541.
- (38) Gao, W.; Liu, W.; Leng, Y.; Wang, X.; Wang, X.; Hu, B.; Yu, D.; Sang, Y.; Liu, H. In₂S₃ nanomaterial as a broadband spectrum photocatalyst to display significant activity. *Appl. Catal. B* **2015**, *176-177*, 83-90.
- (39) Revathi, N.; Prathap, P.; Subbaiah, Y. P. V.; Ramakrishna Reddy, K. T. Substrate temperature dependent physical properties of In₂S₃ films. *J. Phys. D: Appl. Phys.* **2008**, *41*, 155404.
- (40) Wang, S.; Guan, B. Y.; Lu, Y.; Lou, X. W. D. Formation of Hierarchical In₂S₃-CdIn₂S₄ Heterostructured Nanotubes for Efficient and Stable Visible Light CO₂ Reduction. *J. Am. Chem. Soc.* **2017**, *139*, 17305-17308.
- (41) Yang, M.-Q.; Weng, B.; Xu, Y.-J. Synthesis of In₂S₃-CNT nanocomposites for selective reduction under visible light. *J. Mater. Chem. A* **2014**, *2*, 1710-1720.
- (42) Ye, P.; Liu, X.; Iocozzia, J.; Yuan, Y.; Gu, L.; Xu, G.; Lin, Z. A highly stable non-noble metal Ni₂P co-catalyst for increased H₂ generation by g-C₃N₄ under visible light irradiation. *J. Mater. Chem. A* **2017**, *5*, 8493-8498.
- (43) Zhang, N.; Yang, M.-Q.; Tang, Z.-R.; Xu, Y.-J. Toward Improving the Graphene-Semiconductor Composite Photoactivity via the Addition of Metal Ions as Generic Interfacial Mediator. *ACS Nano* **2014**, *8*, 623-633.
- (44) Yue, X.; Yi, S.; Wang, R.; Zhang, Z.; Qiu, S. A novel architecture of dandelion-like Mo₂C/TiO₂ heterojunction photocatalysts towards high-performance photocatalytic hydrogen production from water splitting. *J. Mater. Chem. A* **2017**, *5*, 10591-10598.

- (45) Li, J.-Y.; Li, Y.-H.; Zhang, F.; Tang, Z.-R.; Xu, Y.-J. Visible-light-driven integrated organic synthesis and hydrogen evolution over 1D/2D CdS-Ti₃C₂T_x MXene composites. *Appl. Catal. B* **2020**, *269*, 118783.
- (46) Yang, M.-Q.; Xu, Y.-J.; Lu, W.; Zeng, K.; Zhu, H.; Xu, Q.-H.; Ho, G. W. Self-surface charge exfoliation and electrostatically coordinated 2D hetero-layered hybrids. *Nat. Commun.* **2017**, *8*, 14224.
- (47) Weng, B.; Lu, K.-Q.; Tang, Z.; Chen, H. M.; Xu, Y.-J. Stabilizing ultrasmall Au clusters for enhanced photoredox catalysis. *Nat. Commun.* **2018**, *9*, 1543.
- (48) Ma, B.; Li, X.; Li, D.; Lin, K. A difunctional photocatalytic H₂ evolution composite co-catalyst tailored by integration with earth-abundant material and ultralow amount of noble metal. *Appl. Catal. B* **2019**, *256*, 117865.
- (49) Li, J.; Wang, Y.; Xu, W.; Wang, Y.; Zhang, B.; Luo, S.; Zhou, X.; Zhang, C.; Gu, X.; Hu, C. Porous Fe₂O₃ nanospheres anchored on activated carbon cloth for high-performance symmetric supercapacitors. *Nano Energy* **2019**, *57*, 379-387.
- (50) Perazzolo, V.; Brandiele, R.; Durante, C.; Zerbetto, M.; Causin, V.; Rizzi, G. A.; Cerri, I.; Granozzi, G.; Gennaro, A. Density Functional Theory (DFT) and Experimental Evidences of Metal-Support Interaction in Platinum Nanoparticles Supported on Nitrogen- and Sulfur-Doped Mesoporous Carbons: Synthesis, Activity, and Stability. *ACS Catal.* **2018**, *8*, 1122-1137.
- (51) Garg, A.; Gonçalves, D. S.; Liu, Y.; Wang, Z.; Wang, L.; Yoo, J. S.; Kolpak, A.; Rioux, R. M.; Zanchet, D.; Román-Leshkov, Y. Impact of Transition Metal Carbide and Nitride Supports on the Electronic Structure of Thin Platinum Overlayers. *ACS Catal.* **2019**, *9*, 7090-7098.
- (52) Ponon, N. K.; Appleby, D. J. R.; Arac, E.; King, P. J.; Ganti, S.; Kwa, K. S. K.; O'Neill, A. Effect of deposition conditions and post deposition anneal on reactively sputtered titanium nitride thin films. *Thin Solid Films* **2015**, *578*, 31-37.
- (53) Kaur, M.; Shinde, S. L.; Ishii, S.; Jevasuwan, W.; Fukata, N.; Yu, M. W.; Li, Y.; Ye, J.; Nagao, T. Marimo-Bead-Supported Core-Shell Nanocomposites of Titanium Nitride and Chromium-Doped Titanium Dioxide as a Highly Efficient Water-Floatable Green Photocatalyst. *ACS Appl. Mater Interfaces* **2020**, *12*, 31327-31339.

- (54) Doiron, B.; Li, Y.; Mihai, A.; Bower, R.; Alford, N. M.; Petrov, P. K.; Maier, S. A.; Oulton, R. F. Plasmon-Enhanced Electron Harvesting in Robust Titanium Nitride Nanostructures. *J. Phys. Chem. C* **2019**, *123*, 18521-18527.
- (55) Mashtalyar, D. V.; Sinebryukhov, S. L.; Imshinetskiy, I. M.; Gnedenkov, A. S.; Nadaraia, K. V.; Ustinov, A. Y.; Gnedenkov, S. V. Hard wearproof PEO-coatings formed on Mg alloy using TiN nanoparticles. *Appl. Surf. Sci.* **2020**, *503*, 144062.
- (56) Wang, S. F.; Fu, L. W.; Wei, Y. C.; Liu, S. H.; Lin, J. A.; Lee, G. H.; Chou, P. T.; Huang, J. Z.; Wu, C. I.; Yuan, Y.; Lee, C. S.; Chi, Y. Near-Infrared Emission Induced by Shortened Pt-Pt Contact: Diplatinum(II) Complexes with Pyridyl Pyrimidinato Cyclometalates. *Inorg. Chem.* **2019**, *58*, 13892-13901.
- (57) Lee, J.; Ryou, Y.; Chan, X.; Kim, T. J.; Kim, D. H. How Pt Interacts with CeO₂ under the Reducing and Oxidizing Environments at Elevated Temperature: The Origin of Improved Thermal Stability of Pt/CeO₂ Compared to CeO₂. *J. Phys. Chem. C* **2016**, *120*, 25870-25879.
- (58) Lin, W.; Herzing, A. A.; Kiely, C. J.; Wachs, I. E. Probing Metal-Support Interactions under Oxidizing and Reducing Conditions: In Situ Raman and Infrared Spectroscopic and Scanning Transmission Electron Microscopic-X-ray Energy-Dispersive Spectroscopic Investigation of Supported Platinum Catalysts. *J. Phys. Chem. C* **2008**, *112*, 5942-5951.
- (59) Chen, Z.; Song, Y.; Cai, J.; Zheng, X.; Han, D.; Wu, Y.; Zang, Y.; Niu, S.; Liu, Y.; Zhu, J.; Liu, X.; Wang, G. Tailoring the d-Band Centers Enables Co₄N Nanosheets To Be Highly Active for Hydrogen Evolution Catalysis. *Angew. Chem. Int. Ed.* **2018**, *57*, 5076-5080.
- (60) Li, Z.; Cui, Y.; Wu, Z.; Milligan, C.; Zhou, L.; Mitchell, G.; Xu, B.; Shi, E.; Miller, J. T.; Ribeiro, F. H.; Wu, Y. Reactive metal-support interactions at moderate temperature in two-dimensional niobium-carbide-supported platinum catalysts. *Nat. Catal.* **2018**, *1*, 349-355.
- (61) Cai, F.; Ibrahim, J. J.; Fu, Y.; Kong, W.; Zhang, J.; Sun, Y. Low-temperature hydrogen production from methanol steam reforming on Zn-modified Pt/MoC catalysts. *Appl. Catal. B* **2020**, *264*, 118500.
- (62) Garg, A.; Milina, M.; Ball, M.; Zanchet, D.; Hunt, S. T.; Dumesic, J. A.; Roman-Leshkov, Y. Transition-Metal Nitride Core@Noble-Metal Shell Nanoparticles as Highly CO Tolerant Catalysts. *Angew. Chem. Int. Ed.* **2017**, *56*, 8828-8833.
- (63) Weinert, M.; Watson, R. E. Core-level shifts in bulk alloys and surface adlayers. *Phys. Rev. B* **1995**, *51*, 17168-17180.

- (64) Roca-Ayats, M.; García, G.; Galante, J. L.; Peña, M. A.; Martínez-Huerta, M. V. TiC, TiCN, and TiN Supported Pt Electrocatalysts for CO and Methanol Oxidation in Acidic and Alkaline Media. *J. Phys. Chem. C* **2013**, *117*, 20769-20777.
- (65) Zhao, Q.; Yao, W.; Huang, C.; Wu, Q.; Xu, Q. Effective and Durable Co Single Atomic Cocatalysts for Photocatalytic Hydrogen Production. *ACS Appl. Mater Interfaces* **2017**, *9*, 42734-42741.
- (66) Hou, X.; Cui, L.; Du, H.; Gu, L.; Li, Z.; Yuan, Y. Lowering the schottky barrier of g-C₃N₄/Carbon graphite heterostructure by N-doping for increased photocatalytic hydrogen generation. *Appl. Catal. B* **2020**, *278*, 119253.
- (67) Pendem, C.; Sarkar, B.; Siddiqui, N.; Konathala, L. N. S.; Baskar, C.; Bal, R. K-Promoted Pt-Hydrotalcite Catalyst for Production of H₂ by Aqueous Phase Reforming of Glycerol. *ACS Sustain. Chem. Eng.* **2017**, *6*, 2122-2131.
- (68) Aramendía, M. A.; Benítez, J. A.; Borau, V.; Jiménez, C.; Marinas, J. M.; Ruiz, J. R.; Urbano, F. Study of MgO and Pt/MgO Systems by XRD, TPR, and ¹H MAS NMR. *Langmuir* **1999**, *15*, 1192-1197.
- (69) Yi, T.; Zhang, Y.; Yang, X. Combination of Pt@CeO₂/MCM-56 and CeO₂-CuO/MCM-56 to purify the exhaust emissions from diesel vehicles. *Appl. Catal. A* **2019**, *570*, 387-394.
- (70) Lee, T.; Delley, B.; Stampfl, C.; Soon, A. Environment-dependent nanomorphology of TiN: the influence of surface vacancies. *Nanoscale* **2012**, *4*, 5183-5188.
- (71) Zhang, R. Q.; Lee, T. H.; Yu, B. D.; Stampfl, C.; Soon, A. The role of titanium nitride supports for single-atom platinum-based catalysts in fuel cell technology. *Phys. Chem. Chem. Phys.* **2012**, *14*, 16552-16557.